

Energy Dependence of ϕ Meson Production in Central Pb+Pb Collisions at the CERN-SPS

C. Alt,⁹ T. Anticic,²³ B. Baatar,⁸ D. Barna,⁴ J. Bartke,⁶ L. Betev,¹⁰ H. Bialkowska,²⁰ C. Blume,⁹ B. Boimska,²⁰ M. Botje,¹ J. Bracinić,³ R. Bramm,⁷ P. Bunčić,¹⁰ V. Cerny,³ P. Christakoglou,² P. Chung,¹⁹ O. Chvala,¹⁴ J.G. Cramer,¹⁶ P. Csató,⁴ P. Dinkelaker,⁹ V. Eckardt,¹³ D. Flierl,⁹ Z. Fodor,⁴ P. Foka,⁷ V. Friese,⁷ J. Gál,⁴ M. Gaździcki,^{9,11} V. Genchev,¹⁸ G. Georgopoulos,² E. Gładysz,⁶ K. Grebieszko,²² S. Hegyi,⁴ C. Höhne,⁷ K. Kadija,²³ A. Karev,¹³ D. Kikola,²² M. Kliemant,⁹ S. Kniege,⁹ V.I. Kolesnikov,⁸ T. Kollegger,⁹ E. Kornas,⁶ R. Korus,¹¹ M. Kowalski,⁶ I. Kraus,⁷ M. Kreps,³ D. Kresan,⁷ A. Laszlo,⁴ R. Lacey,¹⁹ M. van Leeuwen,¹ P. Lévai,⁴ L. Litov,¹⁷ B. Lungwitz,⁹ M. Makariev,¹⁷ A.I. Malakhov,⁸ M. Mateev,¹⁷ G.L. Melkumov,⁸ A. Mischke,¹ M. Mitrovski,⁹ J. Molnár,⁴ St. Mrówczyński,¹¹ V. Nolic,²³ G. Pála,⁴ A.D. Panagiotou,² D. Panayotov,¹⁷ A. Petridis*,² W. Peryt,²² M. Pikna,³ J. Pluta,²² D. Prindle,¹⁶ F. Pühlhofer,¹² R. Renfordt,⁹ C. Roland,⁵ G. Roland,⁵ M. Rybczyński,¹¹ A. Rybicki,⁶ A. Sandoval,⁷ N. Schmitz,¹³ T. Schuster,⁹ P. Seyboth,¹³ F. Siklér,⁴ B. Sitar,³ E. Skrzypczak,²¹ M. Slodkowski,²² G. Stefanek,¹¹ R. Stock,⁹ C. Strabel,⁹ H. Ströbele,⁹ T. Susa,²³ I. Szentpétery,⁴ J. Sziklai,⁴ M. Szuba,²² P. Szymanski,²⁰ V. Trubnikov,²⁰ D. Varga,⁴ M. Vassiliou,² G.I. Veres,⁴ G. Vesztergombi,⁴ D. Vranić,⁷ A. Wetzler,⁹ Z. Włodarczyk,¹¹ I.K. Yoo,¹⁵ and J. Zimányi*⁴

(The NA49 collaboration)

¹NIKHEF, Amsterdam, Netherlands.

²Department of Physics, University of Athens, Athens, Greece.

³Comenius University, Bratislava, Slovakia.

⁴KFKI Research Institute for Particle and Nuclear Physics, Budapest, Hungary.

⁵MIT, Cambridge, USA.

⁶Henryk Niewodniczanski Institute of Nuclear Physics, Polish Academy of Science, Cracow, Poland.

⁷Gesellschaft für Schwerionenforschung (GSI), Darmstadt, Germany.

⁸Joint Institute for Nuclear Research, Dubna, Russia.

⁹Fachbereich Physik der Universität, Frankfurt, Germany.

¹⁰CERN, Geneva, Switzerland.

¹¹Institute of Physics Świetokrzyska Academy, Kielce, Poland.

¹²Fachbereich Physik der Universität, Marburg, Germany.

¹³Max-Planck-Institut für Physik, Munich, Germany.

¹⁴Institute of Particle and Nuclear Physics, Charles University, Prague, Czech Republic.

¹⁵Department of Physics, Pusan National University, Pusan, Republic of Korea.

¹⁶Nuclear Physics Laboratory, University of Washington, Seattle, WA, USA.

¹⁷Atomic Physics Department, Sofia University St. Kliment Ohridski, Sofia, Bulgaria.

¹⁸Institute for Nuclear Research and Nuclear Energy, Sofia, Bulgaria.

¹⁹Department of Chemistry, Stony Brook University (SUNYSB), Stony Brook, USA.

²⁰Institute for Nuclear Studies, Warsaw, Poland.

²¹Institute for Experimental Physics, University of Warsaw, Warsaw, Poland.

²²Faculty of Physics, Warsaw University of Technology, Warsaw, Poland.

²³Rudjer Boskovic Institute, Zagreb, Croatia.

ϕ meson production is studied by the NA49 collaboration in central Pb+Pb collisions at 20A, 30A, 40A, 80A and 158A GeV beam energy. The data are compared to measurements at lower and higher energies and to microscopic and thermal models. The energy dependence of yields and spectral distributions is compatible with the assumption that partonic degrees of freedom set in at low SPS energies.

I. INTRODUCTION

The production of strange particles is considered one of the key observables for the understanding of the reaction mechanisms in ultrarelativistic heavy-ion collisions. Enhanced strangeness production with respect to proton-proton collisions has originally been proposed as a signature of the transition to a deconfined state of quarks and gluons during the initial stage of the reactions [1]. The enhancement was predicted to arise from gluon fragmentation into quark-antiquark pairs which is believed to have a significantly lower threshold than strange-antistrange hadron pair

* deceased

production channels. Indeed, it has been observed [2, 3] that the ratio of the number of produced kaons to that of pions is higher by a factor of about two in central S+S and Pb+Pb reactions compared to p+p collisions at top SPS energy.

Statistical hadron gas models have been successfully employed to describe the measured particle yields at various collision energies [4, 5, 6, 7, 8]. The fact that the hadronic final state of the collision resembles a hadron gas in chemical equilibrium has been interpreted as a consequence of the hadronisation process [9] or as a result of a fast hadronic equilibration process involving multi-particle collisions [10]. In this hadron gas picture, enhanced production of strange particles in collisions of large nuclei arises as a consequence of the increased reaction volume, relaxing the influence of strangeness conservation [11]. Technically, this requires the application of the canonical ensemble to small collision systems, while for larger volumes like encountered in central collisions of heavy ions, the grand-canonical approximation is valid. It was shown that this “canonical strangeness suppression” also applies to a partonic system [12].

In addition to this volume effect, the strange particle phase space appears to be undersaturated in elementary interactions. The deviation of the strange particle yields from a hadron gas in full equilibrium was parametrised by a strangeness undersaturation factor γ_S [8, 13]. The additional suppression becomes much weaker in heavy-ion collisions. However, fits to the hadron multiplicities in full phase space are still unsatisfactory when not taking into account γ_S [8]. A possible interpretation is that the total amount of strangeness available for hadronisation is determined in a pre-hadronic stage of the collision. A change in γ_S between p+p and A+A would then reflect the difference in the initial conditions of the respective fireballs.

The hadron gas model was extended to describe the energy dependence of produced hadron multiplicities by a smooth parametrisation of the fit parameters T and μ_B , determined at AGS, top SPS and RHIC energies, as function of collision energy [14]. However, this extended model failed to reproduce the detailed features of the energy dependence of relative strangeness production measured by NA49 in its energy scan programme. In particular, the sharp maximum at around 30A GeV beam energy [15, 16] could not be described. The same holds for microscopic reaction models such as UrQMD [17]. On the other hand, this feature was predicted as a consequence of the onset of a phase transition to a deconfined state at the respective beam energy [18].

In this context, it is certainly interesting to investigate specific strangeness-carrying hadrons. Among these, the ϕ meson is of particular interest due to its $s\bar{s}$ valence quark composition. In a purely hadronic scenario, being strangeness-neutral, it should not be sensitive to hadro-chemical effects related to strangeness. If on the other hand, the amount of available strange quarks is determined in a partonic stage of the collision, the ϕ is expected to react more sensitively than singly strange particles. In particular, one would expect the ϕ yield to be suppressed by γ_s^2 with respect to equilibrium. Analogously, the canonical suppression mechanism in small systems should have a stronger effect on the ϕ , leading to a larger relative enhancement in Pb+Pb collisions with respect to p+p reactions than observed for kaons.

In the evolution of the fireball after hadronisation, ϕ mesons can both be formed by kaon coalescence and destroyed by rescattering. In addition, when decaying inside the fireball, the daughter particles can rescatter, leading to a loss of signal in the invariant mass peak of the respective decay channel. This is more likely to happen for slow ϕ mesons which spend more time in the fireball. Thus the effect could lead to a depletion of the ϕ yield at low p_t in central nucleus-nucleus collisions [19].

Theoretical investigations have suggested that the properties of the ϕ meson might be modified in a dense hadronic medium. In particular, a decrease of its mass of the order of 10 MeV [41] [20] and an increase of its width by a factor of 2-3 [21] were predicted. So far, there is only one experimental claim for a broadening of the width in p+Cu collisions [22].

In an earlier publication [23], we reported on ϕ production at top SPS energy, where we found the ϕ enhanced by a factor of about three, compared to minimum bias pp collisions at the same beam energy. Meanwhile, the ϕ meson was measured at the same energy by the NA50 [24], NA45 [25] and NA60 [26] experiments. At AGS, data on ϕ production were obtained by the E917 collaboration in Au+Au collisions at $p_{beam} = 11.7A$ GeV ($\sqrt{s_{NN}} = 4.88$ GeV) in a restricted rapidity range $[y_{CM} - 0.4, y_{CM}]$ [27]. At RHIC, the STAR collaboration measured the ϕ meson at $\sqrt{s_{NN}} = 130$ GeV and $\sqrt{s_{NN}} = 200$ GeV at midrapidity [28, 29]. For the latter energy, data are also available from the PHENIX experiment [30].

In this article, we report on ϕ production in central Pb+Pb collisions at five different beam energies from 20A to 158A GeV. Together with the data obtained at AGS and RHIC, the energy dependence of ϕ production can thus be studied over a large range of collision energy.

II. THE EXPERIMENT

The NA49 experiment at CERN is based on a fixed-target hadron spectrometer using heavy-ion beams from the SPS accelerator. Its main components are four large-volume time-projection chambers for charged-particle tracking, two

TABLE I: Characteristics of the data sets employed in the analysis

E_{beam} [A GeV]	$\sqrt{s_{NN}}$ [GeV]	y_{beam}	Year	Centrality	$\langle N_w \rangle$	N_{events}	Momentum range [GeV]
20	6.3	1.88	2002	7.2 %	$349 \pm 1 \pm 5$	352,309	2.0 - 23.0
30	7.6	2.08	2002	7.2 %	$349 \pm 1 \pm 5$	368,662	2.0 - 27.0
40	8.8	2.22	1999	7.2 %	$349 \pm 1 \pm 5$	586,768	2.0 - 27.0
80	12.3	2.57	2000	7.2 %	$349 \pm 1 \pm 5$	300,992	2.0 - 32.0
158	17.3	2.91	1996	5.0 %	$362 \pm 1 \pm 5$	345,543	3.5 - 35.0

of which operate inside the magnetic field of two superconducting magnets, thus providing an excellent momentum measurement. Two larger chambers (MTPCs) are placed downstream, outside of the field, and enable particle identification by the measurement of the specific energy loss in the detector gas. The particle identification capabilities are enhanced by a time-of-flight scintillator system behind the MTPCs, albeit in a restricted geometrical acceptance.

A thin lead foil with 1 % interaction probability for Pb nuclei was used as a target. For the different runs, the magnetic field was scaled proportionally to the beam energies in order to have similar acceptance in the CM system.

The centrality of the reactions was determined from the energy deposited by the beam spectators in the zero-degree calorimeter, placed 20 m downstream of the target. By setting an upper limit on this energy, the online central trigger selected the 7.2 % most central collisions at 20A – 80A GeV and the 10 % most central collisions at 158A GeV. The latter data set was restricted to 5 % centrality in the offline analysis. The corresponding mean numbers of wounded nucleons were obtained by Glauber model calculations (see Table I). Details of the experimental apparatus can be found in [31].

III. DATA ANALYSIS

A. Event and track selection

Offline quality criteria were applied to the events selected by the online centrality trigger to suppress non-target interactions, pile-up and incorrectly reconstructed events. The cut variables include the position and χ^2 of the reconstructed vertex and the charged track multiplicity. For the central data sets used in this analysis, however, the impact of these quality cuts is marginal; only about 1 % of all events were rejected. Table I shows the event statistics used in the analysis for the five data sets.

The analysis was restricted to tracks reconstructed in the MTPCs which could be assigned to the primary vertex. A minimal track length of 2 m out of the maximal 4 m in the MTPCs was required to suppress ghost or split tracks and to ensure a good resolution in dE/dx . Detailed studies including reconstruction of simulated tracks embedded into real raw data events showed that for such a selection of tracks, losses due to track reconstruction and high track density are negligible.

B. Selection of kaon candidates

NA49 observes the ϕ meson through its hadronic decay into charged kaons. In order to reduce the large contribution of pions and protons to the combinatorial background, kaon candidates were selected based on their specific energy loss dE/dx in the MTPCs. The mean dE/dx of pions, kaons and (anti-)protons was determined from TOF-identified particles in the acceptance of the time-of-flight detectors and parametrised as a function of $\beta\gamma$ as shown in Fig. 1 (left). This allowed to extend the momentum range for the identification from the TOF acceptance to higher momenta. The lower momentum limit was given by either the MTPC acceptance or the crossing of the Bethe-Bloch curves of pions and kaons. The momentum limits for the different data sets are summarised in Table I.

Fixing the mean dE/dx of kaons and protons to this parametrisation, the resolution was obtained by unfolding the energy-loss spectra in momentum bins into the Gaussian contributions of the particle species (p , K , π and e). The resolution is about 4 % and has a slight momentum dependence which was again parametrised (Fig. 1 (right)).

Kaon candidates were selected by a momentum dependent dE/dx window around the expectation value, the size of which was chosen to optimise the ϕ signal quality. In addition, the window had to be symmetric and large enough to minimise the sensitivity to the errors in the determination of the dE/dx expectation value and resolution. A window

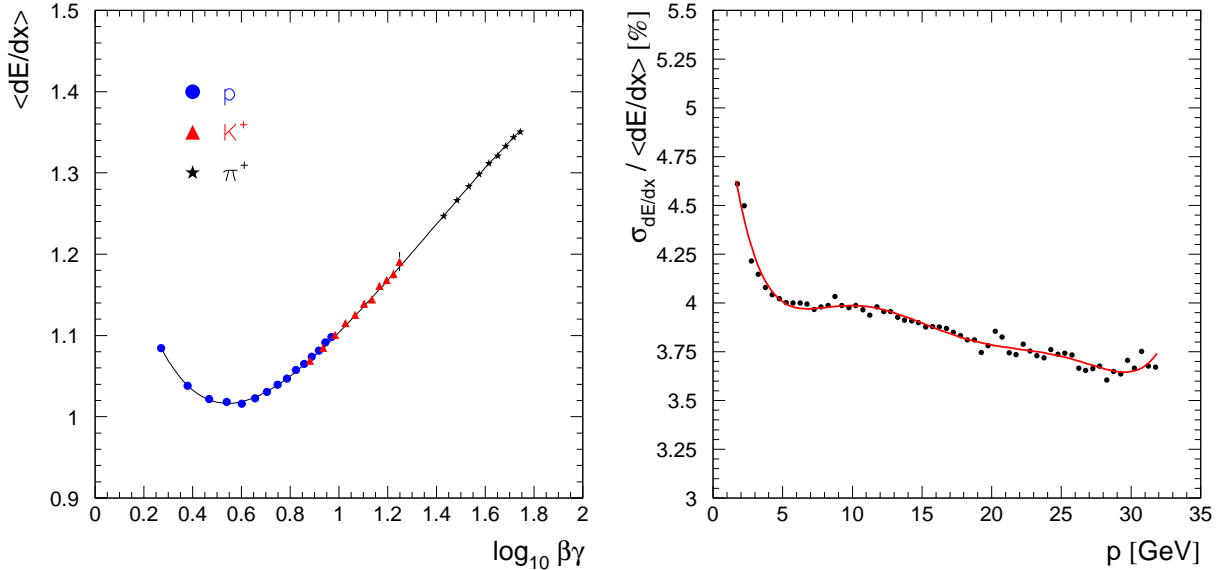


FIG. 1: (Colour online) dE/dx parametrization for the data set at 80A GeV. Left: mean dE/dx as function of $\beta\gamma$ determined for TOF-identified pions, kaons and protons; right: dE/dx resolution as function of momentum, obtained from the deconvolution of the energy loss spectra into the contributions of π^+ , K^+ and p

of $\pm 1.5\sigma$ was found to be the best choice. This selection contains 87% of all kaons, giving an efficiency of 75% for the pair. The fraction of true kaons within the selected candidate track sample varies between 40% and 60%.

C. Extraction of raw yields

The ϕ signal was obtained by calculating the invariant mass of all combinations of positive and negative kaon candidates in one event. To reconstruct the combinatorial background of uncorrelated pairs, candidates from different events were combined. The mixed-event spectrum was subtracted from the same-event spectrum after normalisation to the same number of pairs [32]. Fig. 2 shows the background-subtracted invariant-mass spectra in the total forward acceptance for different collision energies. In all cases, clear signals are observed at the expected position.

While the subtracted spectrum is flat on the right side of the signal, a depletion is observed between the peak and the threshold. As a possible source of this undershoot, the correlation of kaons stemming from different ϕ mesons has been discussed in [32]. In our case, it was shown by simulation that this effect is small due to the large acceptance of the NA49 MTPCs. Another possible source of the distortion is the reflection of other resonances, e.g. $\Delta^0 \rightarrow \pi^- p$, into the K^+K^- spectrum by misidentification of pions and protons, as discussed in detail in [33]. This effect was shown to be present in our previous analysis of another data set [23], where the dE/dx resolution was significantly worse. However, all of such resonances would distort the spectrum over a broad range above threshold, which can be excluded by the observed flatness at higher masses. This conclusion is further strengthened by the observation that the depletion does not vanish when applying a stricter dE/dx cut on the kaons. Hence, the undershoot is likely to originate from a true correlation of kaon pairs. Simulations show that it can be explained by final state strong interaction of kaons [34]. This is demonstrated by Fig. 3 showing the K^+K^- correlation function in $q_{inv} = \sqrt{(\vec{p}_1 - \vec{p}_2)^2 - (E_1 - E_2)^2}$ (left) and in m_{inv} (right). While the repulsive interaction causes a depletion in m_{inv} , the stronger attractive Coulomb effect is squeezed into 0.8 MeV above threshold and is thus hardly seen. In combination with the steeply rising unsubtracted m_{inv} distribution, this depletion can easily account for the deficit observed in the subtracted spectrum.

To correct this effect quantitatively by simulation is difficult and would moreover be model dependent. As the narrow signal is easily distinguished from the broad residual background, we accounted for the depletion by fitting a straight line in the vicinity of the peak. For the description of the signal itself, we used a relativistic p-wave Breit-Wigner distribution [35] of the form

$$\frac{dN}{dm} \propto \frac{m\Gamma(m)}{(m^2 - m_0^2)^2 + m_0^2\Gamma^2(m)} \quad (1)$$

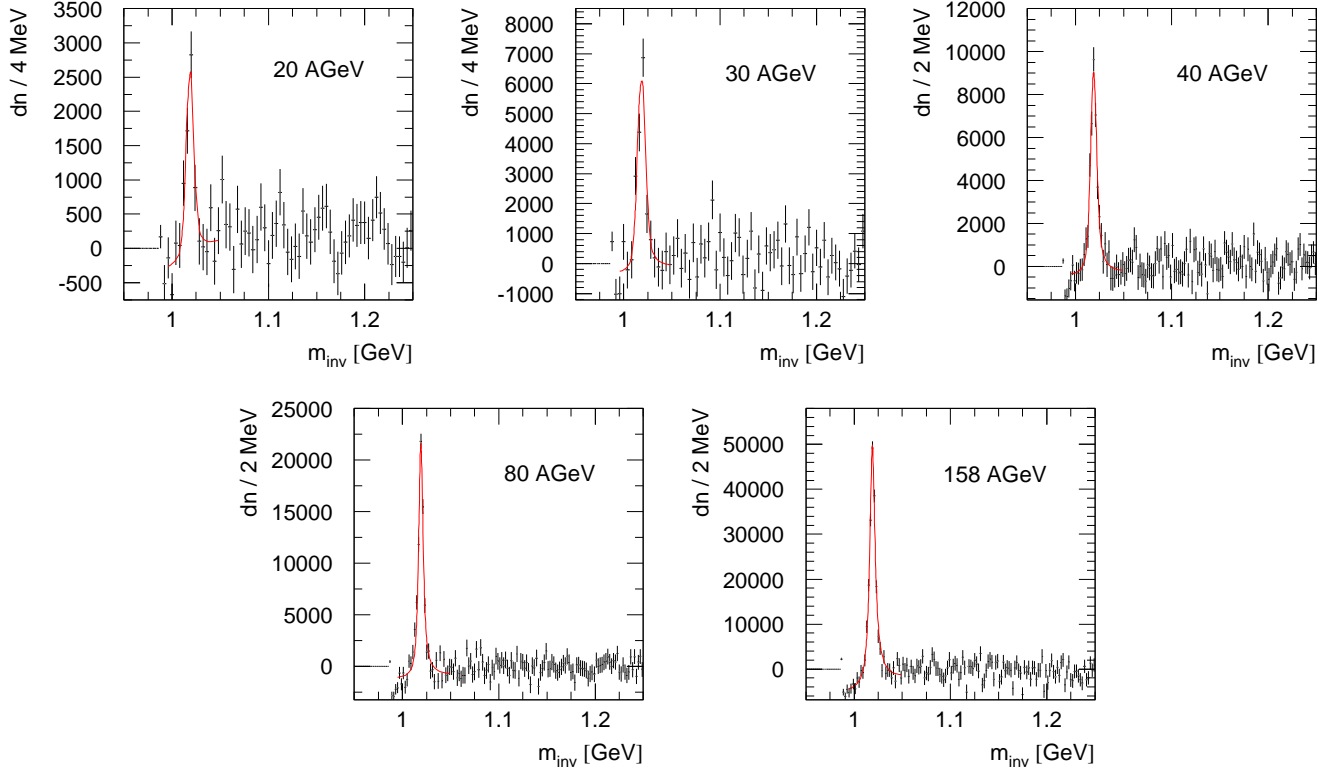


FIG. 2: (Colour online) K^+K^- invariant-mass spectra after subtraction of the combinatorial background in the forward rapidity hemisphere for the five different beam momenta. The full lines show the Breit-Wigner fits to the signals as described in the text. The bin size is 4 MeV for 20A and 30A GeV and 2 MeV for the other beam energies.

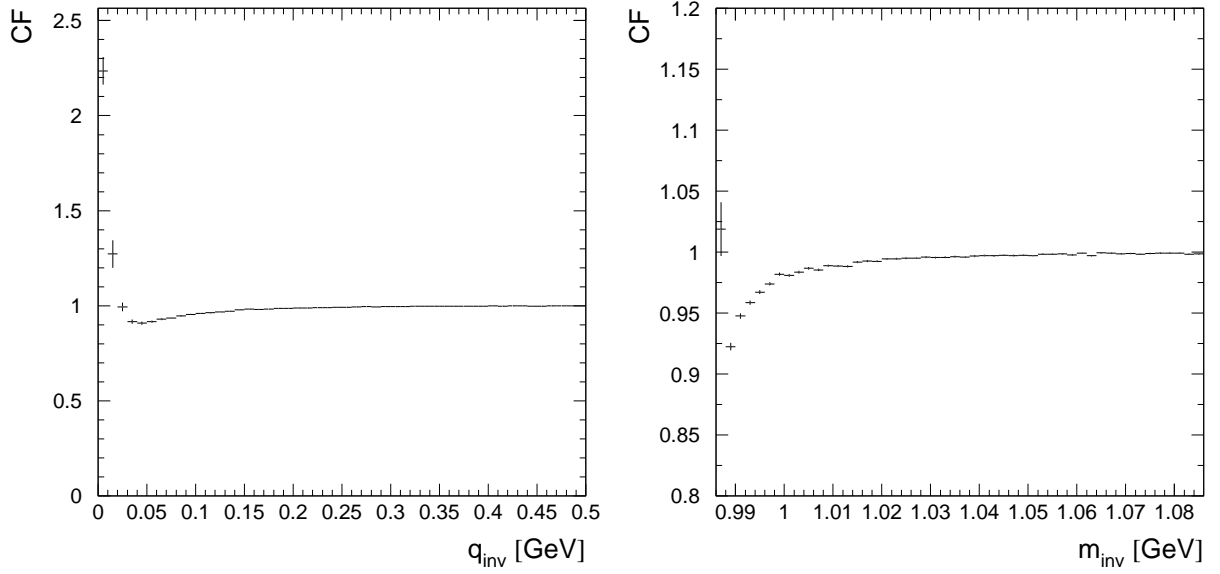


FIG. 3: K^+K^- correlation function close to threshold in q_{inv} (left) and m_{inv} (right) [34]

with the mass-dependent width

$$\Gamma(m) = 2\Gamma_0 \left(\frac{q}{q_0}\right)^3 \frac{q_0^2}{q^2 + q_0^2}, \quad (2)$$

where $q := \sqrt{\frac{1}{4}m^2 - m_K^2}$ and $q_0 := \sqrt{\frac{1}{4}m_0^2 - m_K^2}$. This distribution was folded with a Gaussian representing the invariant-mass resolution σ_m of the spectrometer. Since in general, mass resolution and width cannot be determined separately, we fixed the width to its book value $\Gamma_0 = 4.26$ MeV [36], leaving m_0 , σ_m , a normalisation and two parameters for the linear background as free parameters for the fit, which was performed in the mass range (994 – 1050) MeV. It was checked by simulations that this procedure gives the correct values for position, width and integral of the distribution. As Fig. 2 demonstrates, the fit gives a good description of the signal. The numerical values of the fitted parameters are listed in Table II.

To obtain longitudinal and transverse spectra, the signal was extracted in p_t or rapidity bins in the same way as in the total acceptance. Due to the limited statistics, a two-dimensional binning was not possible, so the transverse distribution was studied integrated over the forward rapidity hemisphere. To reduce the number of free fit parameters, m_0 and σ_m were fixed for the fits in the phase space bins to the values obtained from the signal in the total acceptance. For the 158A GeV data set, where the statistics in the signal allowed to do so, we checked that leaving these parameters free did not significantly alter the results. In particular, no significant dependence of m_0 or σ_m on rapidity or p_t was observed.

Since the straight line background is only an approximation for the residual background in the vicinity of the signal, the stability of the fit against the variation of the fit region was checked. The parameters m_0 and σ_m show no significant dependence. The variation of the normalisation constants, which determine the fit integral, is in all bins far below the statistical error returned by the fit procedure. We conclude that the latter properly takes into account the possible variations of the baseline.

The raw yields in the phase space bins were obtained by integrating the fit function from threshold up to $m_0 + 30\Gamma_0 \approx 1.148$ MeV. This mass cutoff is somehow arbitrary; the corresponding integral varies by about 3 % for cutoff values from $m_0 + 10\Gamma_0$ to infinity. We take this as a systematic uncertainty due to the mass cutoff. Using alternatively a (analytically integrable) non-relativistic Lorentz-Distribution for the fit does not change the integral by more than 1 %.

D. Geometrical acceptance

The geometrical acceptance of the NA49 detector for the decay $\phi \rightarrow K^+K^-$ was obtained double-differentially in y and p_t (integrated over azimuth) by GEANT simulations of the ϕ decay including in-flight decay of the kaon daughters, assuming an azimuthally flat ϕ emission and isotropic decay. The resulting acceptance is shown in Fig. 4 for 20A and 158A GeV. While the upper momentum limit for the daughter candidates restricts the acceptance at forward rapidity for the top SPS energy, at lower beam energies there is lack of acceptance near midrapidity due to the lower momentum limit for the daughter tracks and the increased losses due to in-flight decay for low-momentum kaons.

As the acceptance is a function of y and p_t , the proper correction factor for a given extended phase space bin (integrated either over y or p_t) as used in the analysis is the mean acceptance

$$\bar{a}_S = \frac{\int_S dy dp_t a(y, p_t) f(y, p_t)}{\int_S dy dp_t f(y, p_t)}, \quad (3)$$

where S denotes the region in the y, p_T plane, $a(y, p_t)$ the acceptance probability averaged over the azimuthal angle, and $f(y, p_t)$ the differential ϕ yield. For the rapidity distributions, the differential yields have in addition to be extrapolated to the full p_t range. The extrapolation factor, however, is small (< 5 %) due to the large p_t range covered by the experiment.

Both the acceptance correction and the extrapolation to full p_t require the knowledge of the y and p_t dependence of ϕ yields, which leads to an iterative procedure (see section III E).

E. Spectra and yields

Apart from the differential acceptance correction, the raw yields obtained from the fit to the invariant-mass spectra were corrected for the branching ratio $\phi \rightarrow K^+K^-$ (49.1 %) and the efficiency of kaon dE/dx selection (75 % for the

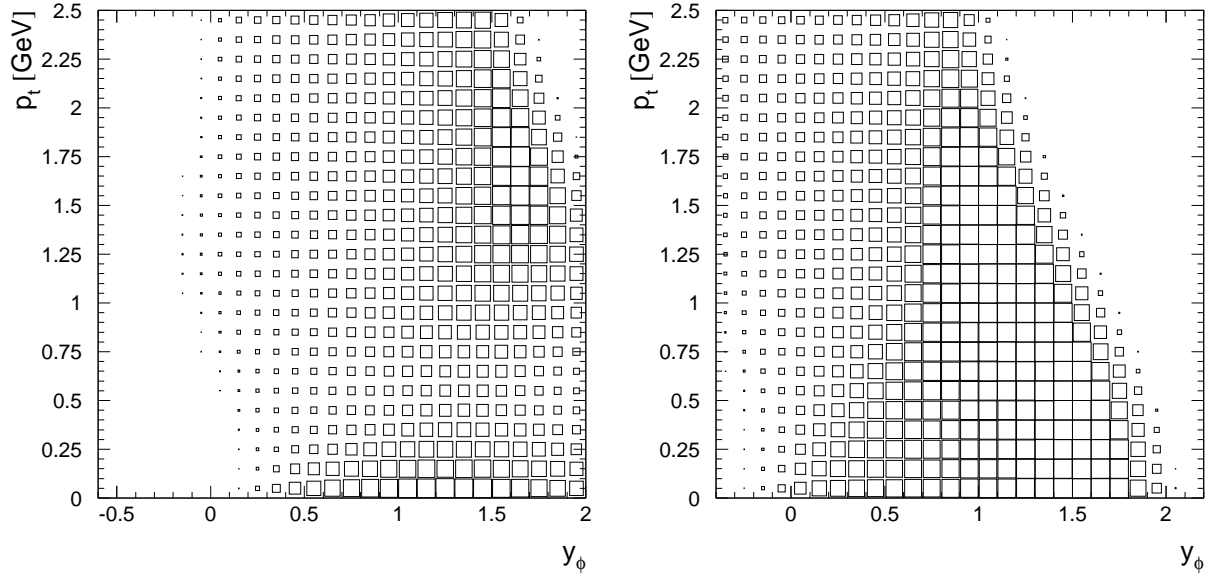


FIG. 4: Geometrical acceptance probability for $\phi \rightarrow K^+K^-$ including kaon decay in flight for 20A GeV (left) and 158A GeV (right).

pair), and normalised to the number of collisions. These global correction factors are common for all bins in phase space and for all beam energies.

The transverse spectra are fitted by the thermal ansatz

$$\frac{dn}{dp_t} \propto p_t e^{-m_t/T}, \quad (4)$$

where the transverse mass $m_t = \sqrt{m_0^2 + p_t^2}$. The distributions in rapidity were parametrised by a single Gaussian

$$\frac{dn}{dy} \propto e^{-\frac{y^2}{2\sigma_y^2}}. \quad (5)$$

As the parameters T and σ_y must be obtained by the analysis itself, an iterative procedure was employed. Starting from some reasonable parameter values, the acceptance correction was calculated according to Eq. (3), assuming factorisation of the emission function $f(y, p_t)$ into the transverse and longitudinal distributions (4) and (5), i. e. independence of T on rapidity. The corrected yields in the p_t and y bins were then fitted with the distributions 4 and 5, respectively, obtaining new values for T and σ_y which serve as input for the next iteration. Convergence of the method was reached after 3 to 5 steps. It was checked that the final results do not depend on the choice of start values for the parameters.

After the final step of the iteration, the yields in full phase space were obtained by summing up the measured yields in the rapidity distributions and numerically extrapolating Eq. (5) to the full rapidity range. In a similar way, the quantities $\langle p_t \rangle$, $\langle m_t \rangle$ and σ_y were determined. The mid-rapidity yield dn/dy was obtained directly from the fit function.

As demonstrated in Fig. 7, the Gaussian parametrisation gives a satisfactory description of the rapidity distribution for all data sets. However, due to the lack of mid-rapidity data points at the lower beam energies, an ambiguity for the extrapolation to full phase space arises. To check the sensitivity of the results on the assumed shape of the rapidity distribution, we alternatively parametrised the latter by the sum of two Gaussian functions displaced symmetrically around mid-rapidity by a shift a :

$$\frac{dn}{dy} \propto e^{-\frac{(y-a)^2}{2\sigma_y^2}} + e^{-\frac{(y+a)^2}{2\sigma_y^2}}. \quad (6)$$

The width of this distribution will be characterised by its RMS value. Total yield $\langle \phi \rangle$, mid-rapidity yield dn_ϕ/dy and RMS_y were calculated for both parametrisations (5) and (6). The final values listed in Tables V and VI were calculated as the mean of the results of the two methods; their differences enter the systematic errors.

F. Statistical and systematic errors

Statistical errors in the raw differential ϕ yields originate from the statistical bin-by-bin errors in the same-event and mixed-event invariant mass spectra, which were found to be in good approximation Poissonian and uncorrelated between mass bins. Then, the statistical errors in the event-mix subtracted invariant-mass spectrum was calculated as [32]

$$\sigma_i^2 = n_{0,i} + k^2 n_{em,i}, \quad (7)$$

where $n_{0,i}$ is the number of entries in mass bin i in the same-event spectrum, $n_{em,i}$ the same number in the mixed-event spectrum, and k the normalisation constant for the event mix. These errors were propagated towards the raw differential yields by the least-squares fit of the Breit-Wigner distribution to the signal peak.

The acceptance calculation was performed with sufficiently high statistics such that the relative statistical error of the differential acceptance is below 1 % and thus far below the uncertainty in the raw yields over the entire y, p_t region used for the analysis. Finally, the errors in the acceptance-corrected differential yields are propagated through the least-square fits to the spectra to obtain the statistical uncertainties in the spectral parameters and the integrated quantities.

Systematic uncertainties in the uncorrected yields arise from the approximation of the residual background in the invariant-mass spectra as a straight line. This approximation is only valid in a limited mass range around the signal peak. Thus, the stability of the results of the Breit-Wigner fit against the variation of the fit range was checked. We found no significant dependence of the parameters m_0 and σ_m ; the variation of the normalisation constant, determining the fit integral, was in all y and p_t bins found to be smaller than the statistical error.

Another source of systematic errors arises from the dE/dx selection of kaon candidates. Uncertainties in the parametrisation of the mean kaon dE/dx and the resolution reflect in systematic deviations of the efficiency correction from its true value. In order to estimate this error, the analysis was repeated for different widths of the dE/dx selection window around the kaon expectation value, applying the respective efficiency correction. This error was found to be the dominating one; it is for most raw yields comparable to or slightly larger than the statistical one.

Imperfect detector description in the simulation leads to systematic uncertainties in the acceptance correction. To reduce possible errors, the analysis was restricted to phase space regions where the acceptance is above 1 %. The remaining error was estimated by repeating the analysis with varying acceptance conditions (minimal track length in the MTPCs). It was in all cases found to be much smaller than the error originating from the kaon selection by dE/dx .

As the spectral parameters enter the acceptance correction through Eq. (3), their uncertainties add to the systematic errors of the corrected yields. This was accounted for by determining the range of acceptance values allowed by the errors in T and σ_y . In addition, for the rapidity bins close to beam rapidity, a possible deviation of the slope parameter by 50 MeV from its averaged value was taken into account in the acceptance correction. The resulting error, however, is small due to the large and approximately uniform p_t acceptance.

The systematic errors in the corrected differential yields were assumed to be independent and added in quadrature. They were propagated to the respective errors in the spectral parameters by repeating the fit of Eqs. (4) - (6) with statistical and systematic errors added and comparing the resulting errors to those obtained from the fit with statistical errors only.

For the determination of the averaged quantities $\langle\phi\rangle$, $\langle p_r\rangle$, $\langle m_t\rangle$ and RMS_y , the summation of the measured differential yields as well as extrapolation to full phase space are required. The systematic errors of these observables were determined from the errors of the differential yields and the uncertainties in the spectral shapes.

IV. RESULTS

A. Line shape

Table II summarises the parameters obtained from the invariant-mass signals in the total acceptance. The signal quality decreases when going to lower beam energy because of both the reduced ϕ yield and the reduced acceptance due to the increased in-flight decay probability for the daughter kaons. At all five energies, the fitted peak position is slightly below the literature value of 1019.43 MeV [36]. We investigated the effect of an error in the normalisation of the magnetic field used for momentum determination in the reconstruction chain and found that a bias of 1 % in the magnetic field is needed to explain the observed shift. This is slightly above the momentum scale uncertainty deduced from a precision study of the K_s^0 signal. We thus cannot exclude that the deviation of the peak position is due to experimental effects.

TABLE II: Approximate number of detected ϕ mesons S , background-to-signal ratio B/S , signal-to-noise ratio SNR , position of the signal peak m_0 and invariant-mass resolution σ_m . The latter two were obtained by a Breit-Wigner fit to the signal peak (see text). The width was fixed to its literature value 4.26 MeV. S and B were calculated in a window of ± 4 MeV around the peak. The quoted errors are statistical only.

p_{beam} [AGeV]	S	B/S	SNR	m_0 [MeV]	σ_m [MeV]
20	6,500	70	9.4	1018.8 ± 0.6	2.6 ± 0.9
30	16,500	104	12.5	1018.4 ± 0.5	2.5 ± 1.3
40	37,000	53	26.2	1018.9 ± 0.2	2.1 ± 0.3
80	55,000	30	42.5	1019.1 ± 0.1	1.1 ± 0.1
158	180,000	72	49.4	1019.0 ± 0.1	1.8 ± 0.1

The widths of the mass peaks obtained from the fits are consistent with those obtained from a full detector simulation and reconstruction. Their slight increase towards lower beam energies can be understood as the increasing influence of multiple scattering on lower momentum tracks. For the signal at 158A GeV, we fitted simultaneously width and mass resolution and obtained $\Gamma_0 = (4.41 \pm 0.61)$ MeV, $\sigma_m = (1.81 \pm 0.26)$ MeV. i. e. no deviation from the free-particle width. Thus, within experimental uncertainties we do not observe indications for a mass shift or a broadening of the ϕ meson.

B. Transverse momentum spectra

The transverse momentum spectra obtained for the five beam energies are shown in Fig. 5; numerical data are given in Table III. In all cases, the thermal distribution (4) gives a good description of the data; the fit parameters are summarised in Table IV. At top SPS energy with the best signal quality, a modest deviation from the fit function is indicated by the χ^2/ndf of 1.5. A slight curvature of the transverse mass spectrum at this energy, as expected from a hydrodynamical expansion scenario, is visible for this energy in Fig. 6 (left). For the other energies, no deviations from pure exponential behaviour can be seen within the experimental uncertainties.

The transverse momentum spectrum can be also characterised by its first moment or the average transverse mass. These parameters were calculated from the measured data points and extrapolated to full p_t using the exponential fit function. As the extrapolation contributes only marginally due to the large p_t coverage, $\langle p_t \rangle$ and $\langle m_t \rangle - m_0$ are largely independent of the spectral shape. Their values are also listed in Table IV.

The assumption of the slope parameter being independent of y could be checked for 158A GeV, where statistics allowed to extract transverse spectra in four different rapidity bins. The resulting slope parameters are shown in Fig. 6 (right). Within the measured rapidity range, we observe no significant change of the slope parameter with y . Using the y dependent slope parameters for correcting the rapidity distribution had no sizeable effect on the results.

The spectrum obtained for 158A GeV agrees with that from an earlier publication [23] of the NA49 experiment, which was based on the analysis of an older data set at the same beam energy. For comparison, the previously published data are shown by the square symbols in Figs. 5 and 6. There is agreement with the results of the CERES experiment in both the decay channels $\phi \rightarrow K^+K^-$ and $\phi \rightarrow e^+e^-$ [25], as also demonstrated in Fig. 6. The data disagree with the spectrum measured by the NA50 experiment in the di-muon decay channel $\phi \rightarrow \mu^+\mu^-$, where a significantly smaller slope was obtained [24].

C. Rapidity distributions and yields

Fig. 7 shows the rapidity distributions, which for all five energies are in good agreement with both the single Gaussian and the double Gaussian parametrisation (see curves). Numerical data are given in Table III. For the data sets at 20A and 30A GeV, due to the low number of data points the double-Gaussian fit was restricted to $a = \sigma_y$ as suggested by the data at 40A and 80A GeV.

Only at 80A GeV the complete forward hemisphere is covered. At 158A GeV large rapidities are not measured because of the upper momentum cut on the secondary kaons. Since kaons below 2 GeV laboratory momentum cannot be reliably identified by dE/dx due to the crossing of the Bethe-Bloch curves, no signal could be extracted at midrapidity for the lower three beam energies. The uncertainties in the extrapolation towards mid-rapidity is demonstrated by the difference of the two parametrisations. It adds to the systematic error of the total yield and,

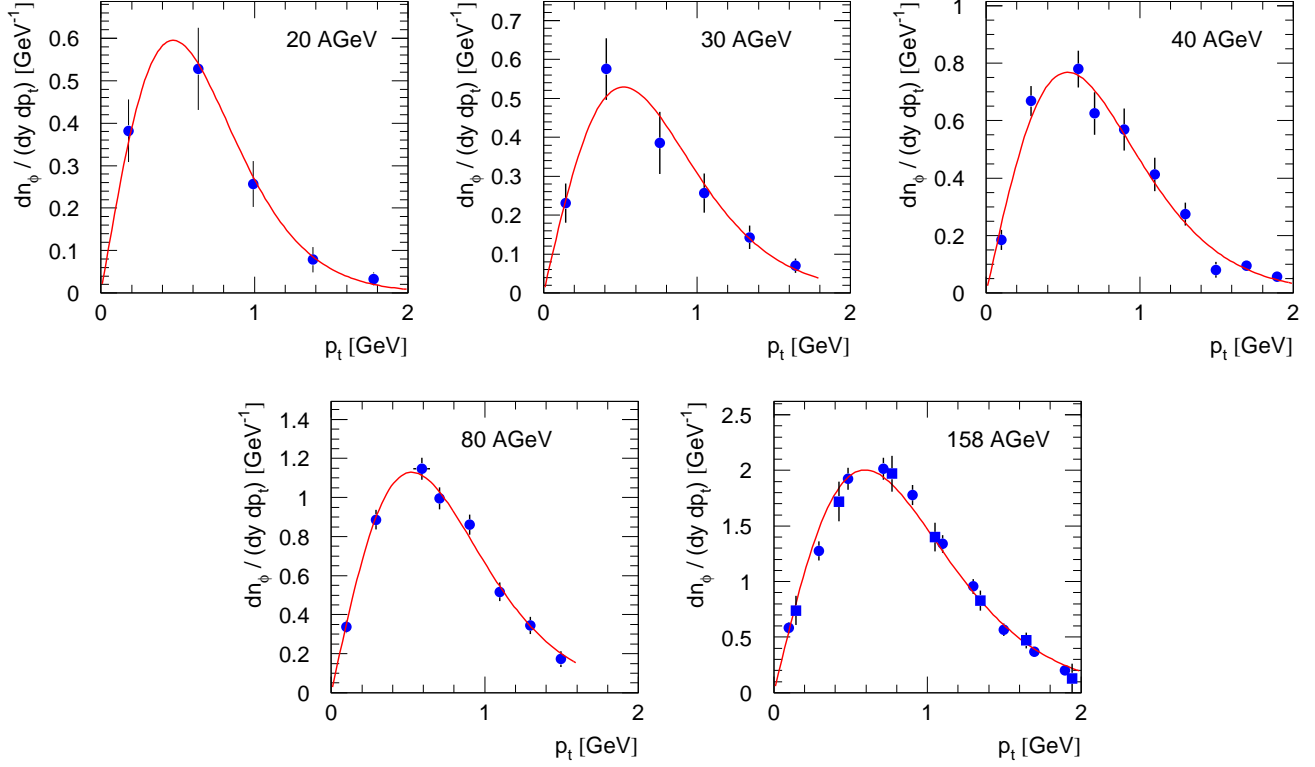


FIG. 5: (Colour online) ϕ transverse momentum spectra integrated over the rapidity intervals given in Table IV. The full lines show the fits of thermal distributions (4). The squared symbols denote previously published results [23]. Only statistical errors are shown.

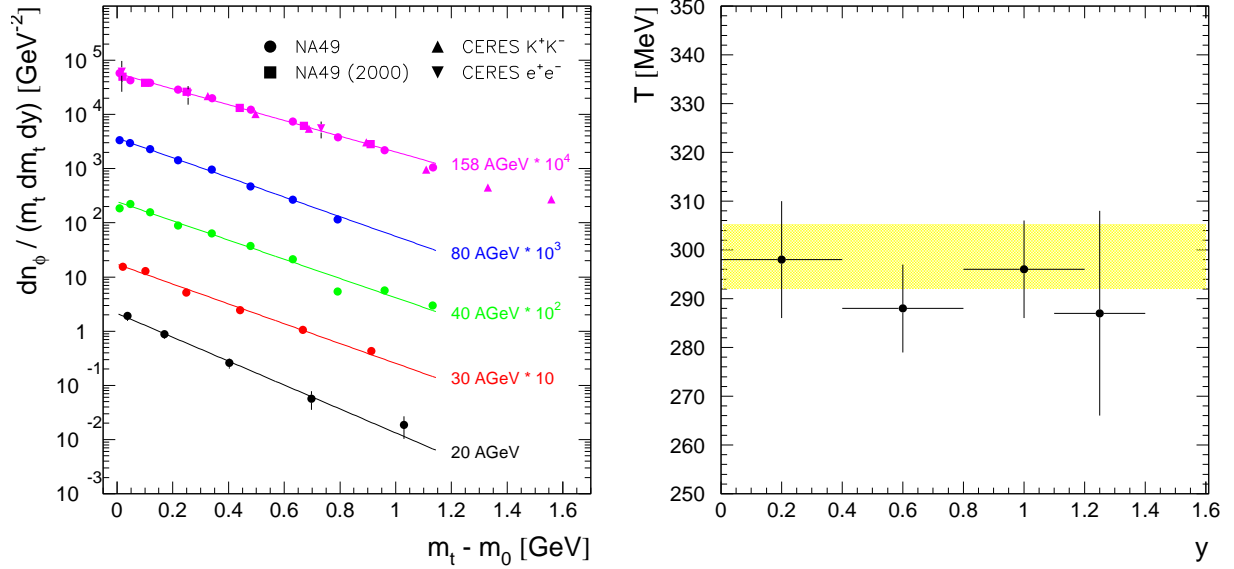


FIG. 6: (Colour online) Left: ϕ transverse mass spectra integrated over the rapidity intervals given in Table IV. The exponential fits indicated by the full lines correspond to the fits shown in Fig. 5. The spectra for different beam energies are scaled for better visibility. Only statistical errors are shown. The data at 158A GeV are compared to previously published results of NA49 [23] and CERES [25]. Right: Slope parameter as function of rapidity at 158A GeV. The shaded area denotes the value obtained integrated over rapidity.

TABLE III: Differential ϕ yields in the (left) p_t and (right) y distributions. Data in the p_t bins are integrated over the rapidity ranges given in Table IV. The errors are statistical.

$E_{beam} = 20A$ GeV			
p_t [GeV]	$dn/(dydp_t)$ [GeV $^{-1}$]	y	dn/dy
0.0 - 0.4	0.382 ± 0.074	0.2 - 0.6	1.043 ± 0.250
0.4 - 0.8	0.528 ± 0.097	0.6 - 1.0	0.536 ± 0.077
0.8 - 1.2	0.257 ± 0.054	1.0 - 1.4	0.159 ± 0.033
1.2 - 1.6	0.079 ± 0.030	1.4 - 1.8	0.032 ± 0.017
1.6 - 2.0	0.033 ± 0.015		
$E_{beam} = 30A$ GeV			
p_t [GeV]	$dn/(dydp_t)$ [GeV $^{-1}$]	y	dn/dy
0.0 - 0.3	0.231 ± 0.051	0.3 - 0.6	0.735 ± 0.194
0.3 - 0.6	0.578 ± 0.079	0.6 - 0.9	0.651 ± 0.090
0.9 - 1.2	0.386 ± 0.079	0.9 - 1.2	0.456 ± 0.052
1.2 - 1.5	0.257 ± 0.050	1.2 - 1.5	0.193 ± 0.036
1.5 - 1.8	0.070 ± 0.019	1.5 - 1.8	0.097 ± 0.029
$E_{beam} = 40A$ GeV			
p_t [GeV]	$dn/(dydp_t)$ [GeV $^{-1}$]	y	dn/dy
0.0 - 0.2	0.185 ± 0.035	0.3 - 0.6	1.067 ± 0.108
0.2 - 0.4	0.668 ± 0.052	0.6 - 0.9	0.756 ± 0.059
0.4 - 0.6	0.780 ± 0.064	0.9 - 1.2	0.611 ± 0.038
0.6 - 0.8	0.625 ± 0.075	1.2 - 1.5	0.348 ± 0.028
0.8 - 1.0	0.569 ± 0.073	1.5 - 1.8	0.188 ± 0.023
1.0 - 1.2	0.413 ± 0.059		
1.2 - 1.4	0.275 ± 0.040		
1.4 - 1.6	0.081 ± 0.028		
1.6 - 1.8	0.086 ± 0.019		
1.8 - 2.0	0.057 ± 0.014		
$E_{beam} = 80A$ GeV			
p_t [GeV]	$dn/(dydp_t)$ [GeV $^{-1}$]	y	dn/dy
0.0 - 0.2	0.337 ± 0.031	-0.3 - 0.0	1.591 ± 0.304
0.2 - 0.4	0.886 ± 0.051	0.0 - 0.3	1.474 ± 0.138
0.4 - 0.6	1.148 ± 0.057	0.3 - 0.6	1.258 ± 0.086
0.6 - 0.8	0.996 ± 0.056	0.6 - 0.9	1.351 ± 0.062
0.8 - 1.0	0.861 ± 0.052	0.9 - 1.2	1.041 ± 0.049
1.0 - 1.2	0.517 ± 0.048	1.2 - 1.5	0.718 ± 0.043
1.2 - 1.4	0.344 ± 0.045	1.5 - 1.8	0.408 ± 0.037
1.4 - 1.6	0.173 ± 0.040	1.8 - 2.1	0.197 ± 0.040
$E_{beam} = 158A$ GeV			
p_t [GeV]	$dn/(dydp_t)$ [GeV $^{-1}$]	y	dn/dy
0.0 - 0.2	0.582 ± 0.053	0.0 - 0.2	2.557 ± 0.166
0.2 - 0.4	1.275 ± 0.086	0.2 - 0.4	2.386 ± 0.121
0.4 - 0.6	1.924 ± 0.098	0.4 - 0.6	2.229 ± 0.098
0.6 - 0.8	2.016 ± 0.099	0.6 - 0.8	2.202 ± 0.089
0.8 - 1.0	1.778 ± 0.092	0.8 - 1.0	1.974 ± 0.090
1.0 - 1.2	1.339 ± 0.080	1.0 - 1.2	1.816 ± 0.094
1.2 - 1.4	0.956 ± 0.067	1.2 - 1.4	1.636 ± 0.105
1.4 - 1.6	0.567 ± 0.055	1.4 - 1.6	1.528 ± 0.126
1.6 - 1.8	0.370 ± 0.044	1.6 - 1.8	1.125 ± 0.171
1.8 - 2.0	0.200 ± 0.034		

in particular, to that of dn/dy at mid-rapidity. Table V lists the parameters obtained by the two fit functions, respectively.

Alternatively, the rapidity distributions can be characterised model independently by their second moments. The root mean square of the distributions was calculated from the measured data and extrapolated to the full rapidity range using the parametrisations (5) and (6). The average of the two results is listed in Table V.

Total yields were obtained by summation of the data points in the rapidity spectra and extrapolation to the full

TABLE IV: Rapidity range (in CM system), p_t range, slope parameter T , χ^2 per degree of freedom, average p_t and average m_t for the transverse momentum spectra. T and χ^2 are results from the fit of Eq. (4) to the spectrum; $\langle p_t \rangle$ and $\langle m_t \rangle - m_0$ are obtained by summation over the data points and extrapolation to full p_t using the fit function. The first error is statistical, the second one systematic.

p_{beam} [AGeV]	y range	p_t range [GeV]	T [MeV]	χ^2/ndf	$\langle p_t \rangle$ [MeV]	$\langle m_t \rangle - m_0$ [MeV]
20	0.0 - 1.8	0.0 - 2.0	$196.8 \pm 19.5 \pm 20.2$	1.06 / 3	$650.9 \pm 34.2 \pm 40.2$	$229.5 \pm 20.1 \pm 23.6$
30	0.0 - 1.8	0.0 - 1.8	$237.4 \pm 17.8 \pm 22.9$	2.03 / 4	$738.9 \pm 28.3 \pm 46.3$	$284.6 \pm 17.3 \pm 28.4$
40	0.0 - 1.5	0.0 - 2.0	$244.6 \pm 9.0 \pm 5.8$	12.42 / 8	$763.4 \pm 15.8 \pm 14.3$	$297.8 \pm 10.0 \pm 9.2$
80	0.0 - 1.7	0.0 - 1.6	$239.8 \pm 8.3 \pm 10.9$	3.48 / 6	$756.4 \pm 11.5 \pm 22.5$	$292.6 \pm 7.6 \pm 15.3$
158	0.0 - 1.0	0.0 - 2.0	$298.7 \pm 6.6 \pm 10.6$	12.06 / 8	$883.5 \pm 9.9 \pm 21.3$	$378.3 \pm 6.7 \pm 15.2$

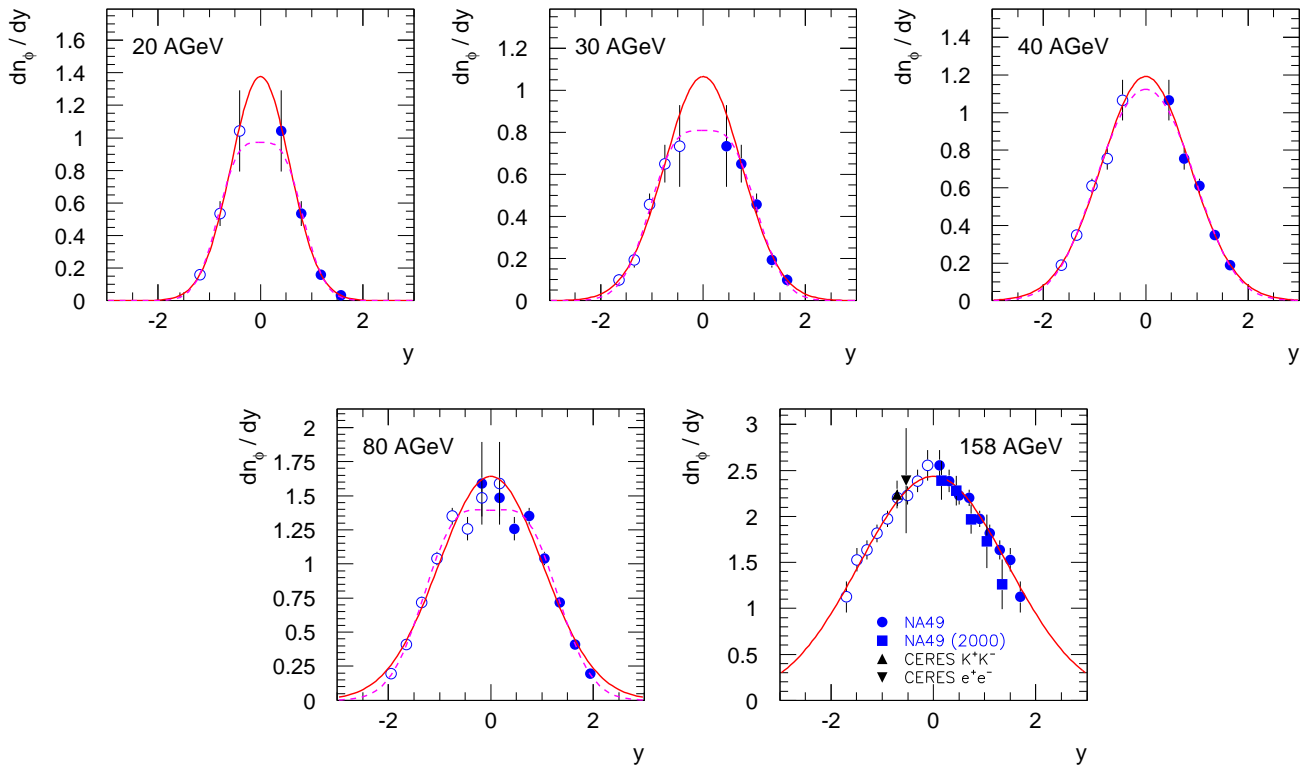


FIG. 7: (Colour online) ϕ rapidity distributions. The solid points refer to measured data, the open points are reflected at midrapidity. The full lines show the parametrisation by a single Gaussian (5), the dashed lines that by the sum of two Gaussians (6). The data at 158A GeV are compared to previously published results of NA49 [23] and CERES [25]. Only statistical errors are shown.

TABLE V: Parameters of the single-Gauss fit (5) and the double-Gauss fit (6) to the rapidity distributions. The RMS was calculated from the data points and extrapolated to the full rapidity range using the average of the two parametrisations. The first error is statistical, the second one systematic.

p_{beam} [AGeV]	σ_1	χ_1^2/ndf	σ_2	a	χ_2^2/ndf	RMS_y
20	$0.572 \pm 0.037 \pm 0.030$	0.042 / 2	$0.425 \pm 0.026 \pm 0.022$	0.425	0.75 / 2	$0.582 \pm 0.031 \pm 0.040$
30	$0.752 \pm 0.047 \pm 0.057$	2.02 / 3	$0.538 \pm 0.028 \pm 0.032$	0.538	1.03 / 3	$0.769 \pm 0.030 \pm 0.062$
40	$0.863 \pm 0.033 \pm 0.042$	3.14 / 4	$0.696 \pm 0.118 \pm 0.036$	$0.487 \pm 0.149 \pm 0.051$	3.10 / 3	$0.852 \pm 0.015 \pm 0.038$
80	$1.016 \pm 0.028 \pm 0.033$	17.55 / 6	$0.658 \pm 0.035 \pm 0.043$	$0.682 \pm 0.029 \pm 0.043$	4.12 / 5	$0.974 \pm 0.024 \pm 0.074$
158	$1.451 \pm 0.086 \pm 0.012$	2.36 / 7				$1.444 \pm 0.021 \pm 0.054$

TABLE VI: Total ϕ multiplicity and mid-rapidity yield dn_ϕ/dy calculated from the rapidity distributions of Fig. 7. The first error is statistical, the second one systematic.

p_{beam} [AGeV]	$\langle\phi\rangle$	$dn_\phi/dy(y_{cm})$
20	$1.89 \pm 0.31 \pm 0.22$	$1.17 \pm 0.23 \pm 0.38$
30	$1.84 \pm 0.22 \pm 0.29$	$0.94 \pm 0.13 \pm 0.30$
40	$2.55 \pm 0.17 \pm 0.19$	$1.16 \pm 0.16 \pm 0.14$
80	$4.04 \pm 0.19 \pm 0.31$	$1.52 \pm 0.11 \pm 0.22$
158	$8.46 \pm 0.38 \pm 0.33$	$2.44 \pm 0.10 \pm 0.08$

rapidity range by the average of the fit functions. The mid-rapidity yield dn/dy was calculated analytically from the average of the fit functions. For the determination of statistical and systematic errors, the correlation of the spectral parameters were properly taken into account. The results for $\langle\phi\rangle$ and dn_ϕ/dy are listed in Table VI.

All results obtained at 158A GeV are consistent within statistical errors with NA49 results published earlier [23], which were obtained from a dataset taken in 1995 (squared symbols in Fig. 7). The main difference of the two datasets is an improved dE/dx resolution, resulting in a reduced pion contamination of the kaon candidate sample. The cleaner kaon identification reduces the distortions in the background-subtracted invariant-mass spectrum induced by resonances with a pion as decay daughter [33], thus leading to a smaller systematic error of the Breit-Wigner fit to the spectrum. We thus prefer to use the newly obtained results at 158A GeV for the discussion.

V. DISCUSSION

The enhancement of relative strangeness production in heavy-ion collisions with respect to proton-proton reactions is a well-known fact. In an earlier publication [23], the enhancement factor for the ϕ meson at top SPS energy was found to be 3.0 ± 0.7 , thus larger than for kaons and Λ , but smaller than for multi-strange hyperons. We calculate the ϕ enhancement by normalising the measured ϕ yield in A+A by the number of wounded nucleon pairs and dividing by the corresponding yield in p+p. As for the lower beam energies no reference measurements in elementary collisions are available, we use a parametrisation of the ϕ excitation function in p+p collisions as described in [27]. For top SPS energy and RHIC, the ϕ yield measured in p+p [23, 29] was used. Fig. 8 shows the resulting enhancement factor

$$E_\phi := \frac{2 \langle\phi\rangle_{A+A}}{N_w \langle\phi\rangle_{p+p}} \quad (8)$$

as function of energy per nucleon pair. The measurement of E917 at AGS ($p_{beam} = 11.7A$ GeV) was extrapolated to full phase space assuming the same rapidity distribution as for K^- as suggested by the authors [27]. We find the ϕ enhancement to be weakly dependent on the collision energy from AGS over the entire SPS energy region; within experimental uncertainties, all data points agree on an enhancement factor of 3 - 4. At RHIC, the enhancement factor appears to be smaller, significantly so, should the PHENIX result be validated. It should be noted, however, that the enhancement factor at RHIC was derived from mid-rapidity data while at lower energies phase-space integrated yields were used.

In the context of statistical models, the enhancement of strangeness production can be interpreted as a result of the release of suppression due to strangeness conservation when going from small (p+p) to large (central A+A) systems. Technically, this is reflected in the application of the canonical ensemble for small systems, while large systems can be described by the grand-canonical ensemble. In this picture, a smaller enhancement at RHIC energies points to the fact that at such high energies, strangeness is produced with sufficient abundance for the canonical suppression to be relaxed even in p+p collisions. However, in a purely hadronic picture canonical suppression does not act on the ϕ meson as it is a strangeness-neutral hadron. Enhanced ϕ production can thus either be attributed to enhanced strangeness production in a partonic stage of the collision or to the coalescence of kaons which suffer canonical suppression also in a hadronic scenario.

The hadro-chemical models have been extended to not only fit hadron multiplicities for a given reaction but to describe the energy dependence of particle yield ratios by a smooth variation of the relevant parameters T and μ_B with collision energy [14, 37]. Here, the energy dependence of temperature and baryo-chemical potential is obtained by a parametrisation of the values for T and μ_B obtained from fits to particle yield ratios at various collision energies. The model reproduces many yield ratios of the bulk hadrons; however, this does not hold for the ϕ meson as shown in Fig. 9, where the measured excitation function of the $\langle\phi\rangle/\langle\pi\rangle$ ratio ($\langle\pi\rangle = 1.5 * (\langle\pi^+\rangle + \langle\pi^-\rangle)$) is compared to the model prediction. The relative ϕ yields at SPS are overpredicted by factors of up to two. The situation remains essentially unchanged when mid-rapidity ratios are considered instead of integrated yields (Fig. 9 (right)). At RHIC, there is

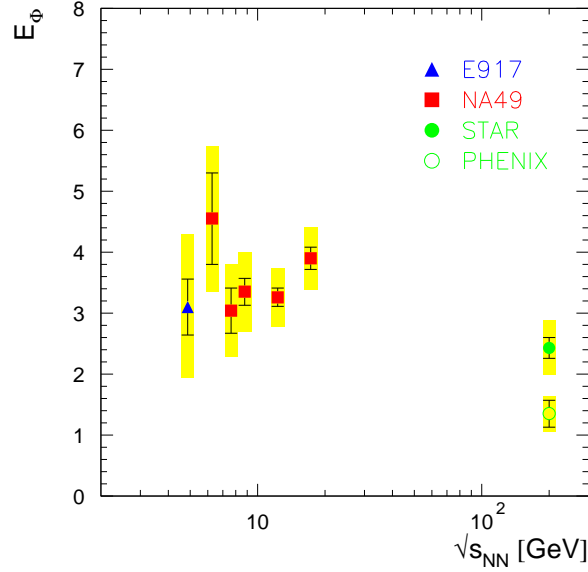


FIG. 8: (Colour online) ϕ enhancement factor E_ϕ (see eq. 8) as function of energy per nucleon pair. Data from AGS [27] and SPS refer to multiplicities in full phase space, data from RHIC [29, 30] to midrapidity yields. The shaded boxes represent the systematic errors.

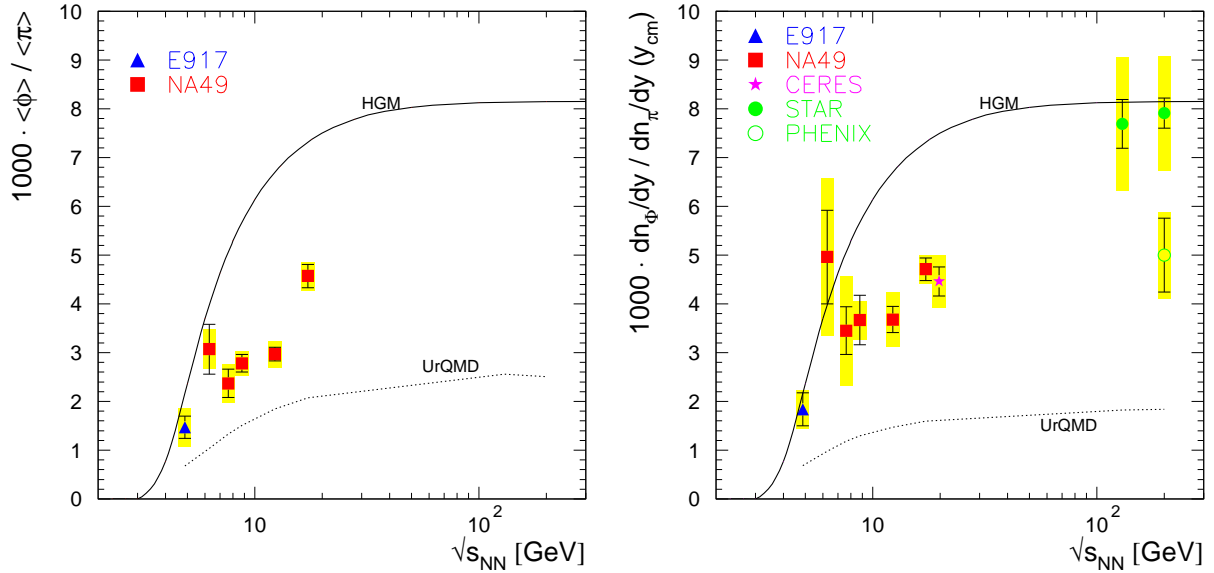


FIG. 9: (Colour online) $\langle\phi\rangle/\langle\pi\rangle$ ratio in full phase space (left) and at mid-rapidity (right) as function of energy per nucleon pair ($\langle\pi\rangle = 1.5(\langle\pi^+\rangle + \langle\pi^-\rangle)$). The CERES data point [25] was displaced horizontally for visibility. Note that the CERES measurement is at $y \approx y_{cm} - 0.5$. The full line shows the predictions of the extended hadron gas model with strangeness equilibration [37], the dashed curves those obtained with UrQMD 1.3 [17]. The shaded boxes represent the systematic errors.

a large experimental ambiguity due to the different results on ϕ production obtained by the STAR and PHENIX experiments [29, 30].

A better description of the data is obtained if a strangeness saturation parameter γ_s is allowed. The corresponding model predictions [8] for the ϕ multiplicity, resulting from a fit to the hadron abundances at 11.7A, 30A, 40A, 80A and 158A GeV, are compared to the data in Fig. 10 (solid points). Note that this model does not provide a continuous description of the energy dependence; the points are only connected to guide the eye. The agreement with the measurements at the higher SPS energies is very good. The successful application of the saturation parameter γ_s

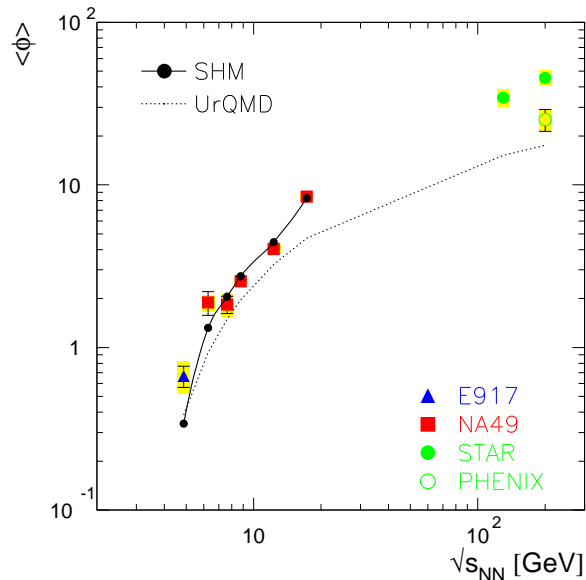


FIG. 10: (Colour online) ϕ multiplicity in central A+A collisions as function of energy per nucleon pair. RHIC mid-rapidity data were scaled to full phase space using the ratio of integrated to mid-rapidity yield obtained with the UrQMD model. The solid points denote the results of the Statistical Hadronization Model (SHM) which allows a deviation from strangeness equilibrium [8]. They are connected by the solid line to guide the eye. The dotted curve shows the ϕ yield predicted by the UrQMD 1.3 model [17]. The shaded boxes represent the systematic errors.

on the strangeness-neutral ϕ meson for $p_{beam} \geq 40A$ GeV again suggests that the strangeness content at chemical freeze-out is determined on a partonic level for these energies.

Final state interactions after chemical freeze-out could change the equilibrium ϕ yield. In particular, scattering of the daughter kaons with other produced hadrons would lead to a loss of the ϕ signal in the experimentally observed decay channel. To study these effects we used the string-hadronic transport model UrQMD [17]. It was found that only about 8 % of the decayed ϕ mesons are lost for detection due to rescattering of their daughter particles, independent of collision energy. Similar results have been obtained with the RQMD model [19]. The effect is thus not sufficient to account for the deviation of the relative ϕ multiplicities from their equilibrium values.

On the other hand, ϕ mesons can be produced by KK scattering. In fact, kaon coalescence is the dominant ($\approx 70\%$) production mechanism for the ϕ in UrQMD, again for all investigated collision systems. As shown by the dotted curve in Fig. 10, the model gives a reasonable description of the ϕ yields at lower energies while it starts to deviate from the measurements at intermediate SPS energies. The discrepancy with data is more pronounced when studying the $\langle \phi \rangle / \langle \pi \rangle$ ratio (Fig. 9) due to the fact that UrQMD overestimates the pion yields at SPS energies by about 30 %.

The hypothesis that the ϕ meson is produced predominantly by kaon coalescence can be tested by comparing the ϕ and kaon distributions in phase space. Fig. 11 (left) shows the width of the ϕ rapidity distribution as function of beam rapidity at SPS energies, together with that measured for π^- , K^+ , and K^- [38, 39]. The ϕ meson width does not fit into the systematics observed for the other particle species, but increases much faster with energy. While at 20A GeV, the ϕ rapidity distribution is narrower than that of K^- , we find it at top SPS energy comparable to the pions. In addition, at 158A GeV it is much larger in central Pb+Pb collisions than measured in p+p collisions at the same energy [23], a feature which is not observed for other particle species.

In the kaon coalescence picture, there would be a tendency for the ϕ rapidity distribution to be narrower than those of the kaons. In an ideal case, neglecting correlations,

$$\frac{1}{\sigma_\phi^2} = \frac{1}{\sigma_{K^+}^2} + \frac{1}{\sigma_{K^-}^2}, \quad (9)$$

where the distributions were approximated by Gaussians. As shown in Fig. 11 (right), the ϕ data rule out kaon coalescence to predominate from 30A GeV on, while at lower energies, the observed rapidity widths are consistent with the coalescence being the dominant formation mechanism. As mentioned before, this would also explain the ϕ enhancement at low energies, where a transient deconfined state is not expected.

The observation that models based on a purely hadronic reaction scenario have serious problems in describing relative strangeness production in the upper SPS energy range is not unique to the ϕ meson but holds for kaons and

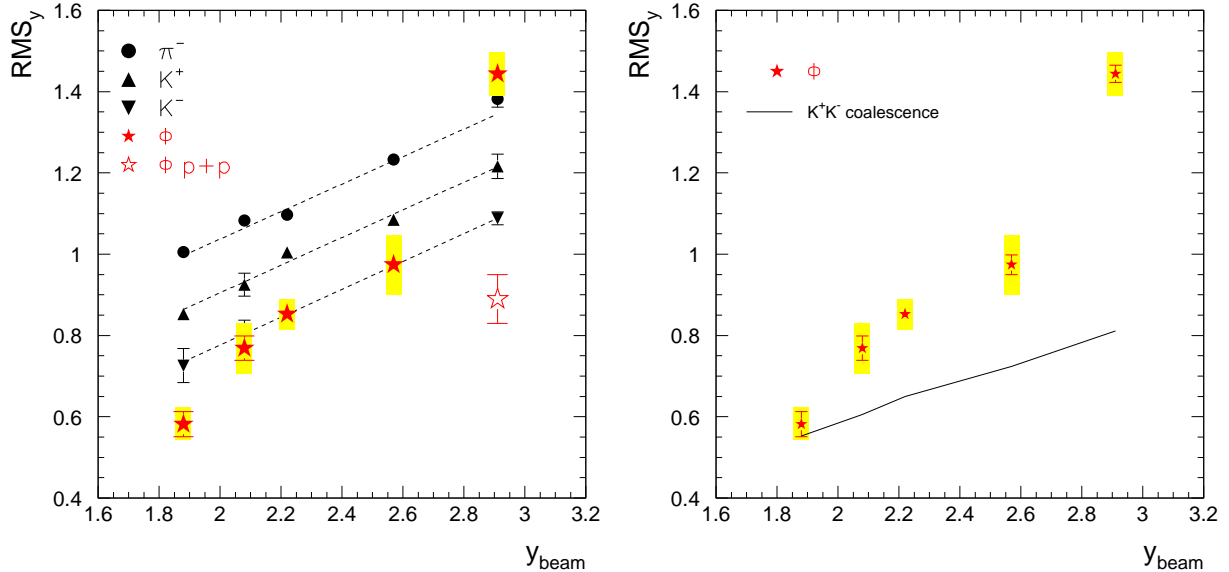


FIG. 11: (Colour online) Left: Widths of the rapidity distributions of π^- , K^+ , K^- , and ϕ in central Pb+Pb collisions at SPS energies as function of beam rapidity [38, 39]. The dashed lines are to guide the eye. The open star denotes the ϕ rapidity width measured in p+p collisions [23]. Right: Widths of the ϕ rapidity distributions in central Pb+Pb collisions compared to the expectations in a kaon coalescence picture (Eq. (9)). The shaded boxes represent the systematic errors (shown only for ϕ mesons).

other strange particles, too. It has been related to the onset of deconfinement at around $30A$ GeV as predicted by the Statistical Model of the Early Stage [18]. A striking experimental evidence is the narrow maximum in the K^+/π^+ ratio at this energy [38, 39]. A similar structure is, within experimental errors, not observed for the ϕ meson (Fig. 9); instead, the energy dependence of the relative ϕ yield resembles that of the K^- . This can be understood since the K^+ yield is in good approximation proportional to the total strangeness production, which is not the case for K^- and ϕ as a large, energy-dependent fraction of s quarks is carried by hyperons.

A second experimental evidence for a deconfinement phase transition is the independence of slope parameters or mean transverse mass from collision energy, seen in the SPS energy range for pions, kaons and protons [39], which can be attributed to the mixed phase of a first-order phase transition [40]. The energy dependences of both the inverse slope parameter and the mean transverse mass of the ϕ meson are shown in Fig. 12. The transverse mass spectra of the ϕ are well described by exponential fits (see Fig. 6); consequently, the two parameters show a similar behaviour. The situation is less clear than in the case for the other hadrons due to the lack of data at lower AGS energies; however, within the experimental uncertainties the energy dependence of the spectral shape is similar to that observed for pions, kaons and protons, with the exception of the data point at top SPS energy where the inverse slope parameter is significantly larger than at lower energies.

VI. SUMMARY

We have presented new data on ϕ production in central Pb+Pb collisions obtained by the NA49 experiment at $20A$, $30A$, $40A$, $80A$ and $158A$ GeV beam energy. The energy dependence of the production characteristics was studied by comparing with measurements at AGS and RHIC energies. We find that at low SPS energy, the data can be understood in a hadronic reaction scenario while at higher energies, hadronic models fail to reproduce the data. Here, a statistical hadron gas model with undersaturation of strangeness gives a good description of the measured yields, which suggests that ϕ production is ruled by partonic degrees of freedom. In summary, our results are consistent with an onset of deconfinement at lower SPS energy as indicated by data on pion and kaon production.

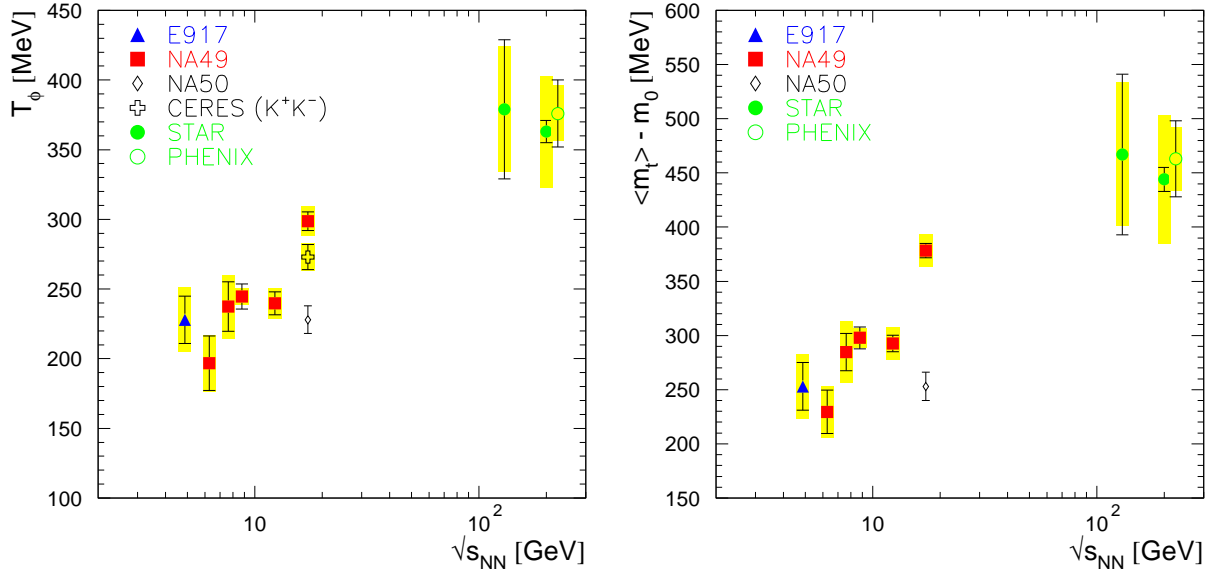


FIG. 12: (Colour online) Inverse slope parameter T (left) and average transverse mass $\langle m_t \rangle - m_0$ (right) of the ϕ meson in central A+A collisions as function of energy per nucleon pair. The data from E917 [27] were averaged over the measured rapidity interval (see Table IV). Results from NA50 [24] and RHIC [28, 29, 30] were obtained at mid-rapidity, the result from CERES at $y = -0.71$. Data from NA49 are integrated over rapidity. The PHENIX data point was slightly displaced horizontally for visibility. For the NA49 data, $\langle m_t \rangle$ was calculated from the transverse momentum spectra using an exponential extrapolation to full p_t . For the other data sets it was derived analytically from the exponential fit function. The shaded boxes represent the systematic errors.

Acknowledgements

This work was supported by the US Department of Energy Grant DE-FG03-97ER41020/A000, the Bundesministerium für Bildung und Forschung, Germany, the Polish State Committee for Scientific Research (2 P03B 006 30, SPB/CERN/P-03/Dz 446/2002-2004, 2 P03B 04123), the Hungarian Scientific Research Foundation (T032648, T032293, T043514), the Hungarian National Science Foundation, OTKA, (F034707), the Polish-German Foundation, and the Korea Research Foundation Grant (KRF-2003-070-C00015).

References

- [1] P. Koch, B. Müller and J. Rafelski, Phys. Rep. **142** (1986) 167
- [2] J. Bartke *et al.*, Z. Phys. C **48** (1990) 191
- [3] F. Sikler (for the NA49 collaboration), Nucl. Phys. A **661** (1999) 45c
- [4] J. Cleymans and K. Redlich, Phys. Rev. C **60** (1999) 054908
- [5] P. Braun-Munzinger, I. Heppe and J. Stachel, Phys. Lett. B **465** (1999) 15
- [6] P. Braun-Munzinger *et al.*, Phys. Lett. B **518** (2001) 41
- [7] R. Averbek *et al.*, Phys. Rev. C **67** (2003) 024903
- [8] F. Becattini, J. Manninen and M. Gaździcki, Phys. Rev. C **73** (2006) 044905
- [9] R. Stock, Phys. Lett. B **456** (1999) 277
- [10] P. Braun-Munzinger, J. Stachel and C. Wetterich, Phys. Lett. B **596** (2004) 61
- [11] R. Hagedorn and K. Redlich, Z. Phys. C **27** (1985) 541
- [12] J. Rafelski and M. Danos, Phys. Lett. B **97** (1980) 279
- [13] F. Becattini and U. Heinz, Z. Phys. C **76** (1997) 269
- [14] P. Braun-Munzinger *et al.*, Nucl. Phys. A **697** (2002) 902
- [15] M. Gaździcki *et al.*, J. Phys. G **30** (2004) S701
- [16] V. Friese *et al.*, J. Phys. G **31** (2005) S911
- [17] M. Bleicher *et al.*, J. Phys. G **25** (1999) 1859

- [18] M. Gaździcki and M. Gorenstein, *Acta Phys. Polon. B* **30** (1999) 2705
- [19] S. C. Johnson, B. V. Jacak and A. Drees, *Eur. Phys. J. C* **18** (2001) 645
- [20] T. Hatsuda and S. Lee, *Phys. Rev. C* **46** (1992) R34
- [21] D. Lissauer and E. V. Shuryak, *Phys. Lett. B* **253** (1991) 15
- [22] R. Muto *et al.*, *Phys. Rev. Lett.* **98** (2007) 042501
- [23] S. Afanasiev *et al.*, *Phys. Lett. B* **491** (2000) 59
- [24] B. Alessandro *et al.*, *Phys. Lett. B* **555** (2003) 147
- [25] D. Adamová *et al.*, *Phys. Rev. Lett.* **96** (2006) 152301
- [26] A. de Falco *et al.*, *Nucl. Phys. A* **774** (2006) 719
- [27] B. B. Back *et al.*, *Phys. Rev. C* **69** (2004) 054901
- [28] C. Adler *et al.*, *Phys. Rev. C* **65** (2002) 041901(R)
- [29] J. Adams *et al.*, *Phys. Lett. B* **612** (2005) 181
- [30] S. S. Adler *et al.*, *Phys. Rev. C* **72** (2005) 014903
- [31] S. Afanasiev *et al.*, *Nucl. Instr. and Meth. A* **430** (1999) 210
- [32] D. Drijard and H. G. Fischer, *Nucl. Instr. and Meth. A* **225** (1984) 367
- [33] V. Friese, Dissertation, Universität Marburg 1999, <https://edms.cern.ch/document/816025/1>
- [34] R. Lednicki, private communication
- [35] J. D. Jackson, *Nuov. Cim.* **34** (1964) 1644
- [36] S. Eidelmann *et al.*, *Phys. Lett. B* **592** (2004) 1
- [37] A. Andronic, P. Braun-Munzinger and J. Stachel, *Nucl. Phys. A* **772** (2006) 167
Data provided by A. Andronic
- [38] S. V. Afanasiev *et al.*, *Phys. Rev. C* **66** (2002) 054902
- [39] C. Alt *et al.*, *Phys. Rev. C* **77** (2008) 024903
- [40] M. Gorenstein, M. Gaździcki and K. Bugaev, *Phys. Lett. B* **567** (2003) 175
- [41] For better readability, we use natural units, i. e. $c = 1$, throughout this article.